



Origin of the Solar Rotation Harmonics Seen in the EUV and UV Irradiance

G. Giono¹ · J.J. Zender² · R. Kariyappa^{3,4} · L. Damé⁵

Received: 5 March 2021 / Accepted: 25 October 2021 / Published online: 25 November 2021
© The Author(s) 2021

Abstract

Long-term periodicities in the solar irradiance are often observed with periods proportional to the solar rotational period of 27 days. These periods are linked either to some internal mechanism in the Sun or said to be higher harmonics of the rotation without further discussion of their origin. In this article, the origin of the peaks in periodicities seen in the solar extreme ultraviolet (EUV) and ultraviolet (UV) irradiance around the 7, 9, and 14 days periods is discussed. Maps of the active regions and coronal holes are produced from six images per day using the Spatial Possibilistic Clustering Algorithm (SPoCA), a segmentation algorithm. Spectral irradiance at coronal, transition-region/chromospheric, and photospheric levels are extracted for each feature as well as for the full disk by applying the maps to full-disk images (at 19.3, 30.4, and 170 nm sampling in the corona/hot flare plasma, the chromosphere/transition region, and the photosphere, respectively) from the Atmospheric Imaging Assembly (AIA) on board the Solar Dynamics Observatory (SDO) from January 2011 to December 2018. The peaks in periodicities at 7, 9, and 14 days as well as the solar rotation around 27 days can be seen in almost all of the solar irradiance time series. The segmentation also provided time series of the active regions and coronal holes visible area (i.e. in the area observed in the AIA images, not corrected for the line-of-sight effect with respect to the solar surface), which also show similar peaks in periodicities, indicating that the periodicities are due to the change in area of the features on the solar disk rather than to their absolute irradiance. A simple model was created to reproduce the power spectral density of the area covered by active regions also showing the same peaks in periodicities. Segmentation of solar images allows us to determine that the peaks in periodicities seen in solar EUV/UV irradiance from a few days to a month are due to the change in area of the solar features, in particular, active regions, as they are the main contributors to the total full-disk irradiance variability. The higher harmonics of the solar rotation are caused by the clipping of the area signal as the regions rotate behind the solar limb.

Keywords EUV and UV radiation · Periodicity · Segmentation

1. Introduction

Investigation of periodicities in solar observational data from both ground-based and satellite space missions has long been of high interest to understand the solar variability. The

Extended author information available on the last page of the article

existence of a long-term cycle of about 11 years and short-term period of 27 days has been well established using numerous solar indices. These periods are associated with the solar magnetic activity and the modulation of solar features on the surface due to the solar rotation. It is important to search for other possible periodicities in solar data, since the detection of any periodicity in active phenomena would have fundamental significance in understanding of the solar activity. Further, it is assumed that solar irradiance is the main driver for the energy budget to affect the Earth's climate and space weather, thus these investigations may improve the understanding of the solar-terrestrial effects and relationships.

Using time-series analysis of various solar indices, many authors have found the 27-day period in relative sunspot numbers, 10.7 cm radio flux data, solar UV irradiance, and geomagnetic indices (e.g., Simon, 1982; Donnelly, Heath, and Lean, 1982; Donnelly et al., 1983; Rottman, 1983; Rottman and London, 1984; Simon et al., 1987; Lean and Brueckner, 1988; Tobiska and Bouwer, 1989; Barth, Tobiska, and Rottman, 1990). In addition, it has been reported by several authors that the ultraviolet spectral irradiance shows a prominent period around 13.5 days, but it has not been shown in the 10.7 cm radio flux (Donnelly, Heath, and Lean, 1982; Donnelly et al., 1983).

However, the real physical origin of these periods needs still to be known and it requires further detailed investigations using long based time-series data. The previous results were based on data sets that are not long enough to get any statistically significant periods, and these long periods may originate from the computational techniques used, such as the way of data detrending and smoothing. The existence of these periods depends strongly on the solar activity and the time interval that has been investigated. This would suggest a quasi-periodic or time-varying behavior rather than a real cyclic one of various solar data. The various periods have been derived from the integrated irradiance observations but not from spatially resolved full-disk segmented features from the images. As it is important to show the real origin of the longer periodicities, further studies are required using spatially resolved images of the Sun obtained at different wavelengths and the corresponding different segmented magnetic features, particularly, for longer-period observations. Recently, we have published several papers on the segmentation of coronal and photospheric features and their time series using spatially resolved full-disk images of the Sun observed from the Atmospheric Imaging Assembly (AIA) and the Helioseismic and Magnetic Imager (HMI), both on board the Solar Dynamics Observatory spacecraft (SDO), as well as the Sun Watcher using APS and Image Processing (SWAP) and the Large Yield Radiometer (LYRA), both on board the PROBA2 spacecraft to understand the extreme ultraviolet (EUV) and ultraviolet (UV) irradiance variability (Kumara et al., 2012, 2014; Zender et al., 2017).

In this article, using SDO/AIA data, we discuss the existence of different periodicities observed in the EUV and UV irradiance from the different atmospheric layers, from the photosphere to the corona. Section 2 describes the data processing and segmentation method applied on full-disk images used for this analysis. The spectral analysis presented in Section 3 shows similar peaks of periodicities at 7, 9, and 14 days in the solar irradiance. However, Section 4 provides evidence that the periodicities are induced by the variability in the total area covered by features on the solar surface (mainly active regions but also coronal holes). A wavelet analysis presented in Section 5 also reveals that the periodicities are not always present at all times, and a second spectral analysis did not actually reveal any particular underlying periodic pattern, indicating that the solar features are generated following a random process (on time-scales up to a month). Finally, using simple models in Section 6, we demonstrate that most of the observed peaks in periodicities are naturally derived as higher-order harmonics of the solar rotation introduced by the clipped signal of the visible area of the features, as they go outside the observer's field-of-view (i.e. behind the Sun).

2. Data Processing

Full-disk images from the Atmospheric Imaging Assembly (AIA, Lemen et al., 2012) on board the Solar Dynamics Observatory (SDO, Pesnell, Thompson, and Chamberlin, 2011) were used for the analysis. Three spectral pass-bands were selected in the EUV and UV: 19.3, 30.4, and 170 nm to sample the corona/hot flare plasma (1.2×10^6 and 2×10^7 K), the chromosphere/transition region (5×10^4 K), and the photosphere (5×10^3 K), respectively. Six of each images were taken per day (i.e. 4 h cadence) from 1 January 2011 to 31 December 2018. The Spatial Possibilistic Clustering Algorithm (SPoCA, Barra, Delouille, and Hochedez, 2008; Barra et al., 2009; Verbeeck et al., 2014) was applied to obtain maps of the active regions and coronal holes. SPoCA uses AIA images from two coronal emission lines for the segmentation: 17.1 nm, where the active regions are prominently seen, and 19.3 nm, where the coronal holes can be clearly observed. The level 1.5 AIA images of 4096 by 4096 pixels were used as input for the SPoCA algorithm in our own data pipeline (executed daily on our local server at the European Space Research and Technology Center (ESTEC) since 2012, using the version of SPoCA classification algorithm from May 2012). The maps were then scaled down to 1024 by 1024 pixels at 19.3, 30.4 and 170 nm for the analysis. The reader is invited to look through a paper by Kumara et al. (2014) for a visual example of the segmented images. A quiet-Sun region was defined as all pixels inside the solar disk but not belonging to either the active regions or the coronal holes maps, and the full disk was taken as the entire integrated image. The total number of counts extracted can then be converted into photon flux by dividing by the AIA peak channel response taken from the IDL AIA SolarSoft (SSW) package (`aia_get_response` routine) and by the image exposure time taken from the fits header. The signal was further corrected for the degradation of the throughput over time also tabulated in the IDL AIA SSW package (`aia_bp_get_corrections` routine). The resulting time-series were also corrected for discontinuities, which occurred several times during the 7-year period due to changes in the flat-field (AIA team, private communication). These discontinuities are mostly seen in the 30.4 and 170 nm channels, for which they were corrected by imposing continuity of the signal. Finally, to account for the changing distance between the Earth and the Sun during the year, the measured flux was normalized to a distance of 1 AU using the Horizons Ephemeris Service.¹ Figure 1 shows the obtained time-series for the total flux of the full disk and of the segmented features (active regions, coronal holes, and quiet Sun) for three different atmospheric layers. It is important to point out that the AIA images fed to the SPoCA algorithm were not corrected for the degradation, which might have slightly affected the segmentation towards the end of the 2011–2018 period.

3. Periodicity in the Solar Irradiance

A spectral analysis was performed on each of the time-series shown in Figure 1. The power spectral density (PSD) was computed by the Welch method: the entire timeline was subdivided in half-overlapping segments ≈ 200 days long (1/8 of the total timeline), a Fourier transform was performed on each of the segments after detrending (i.e. subtraction of a linear fitting), a Hann window was applied to the time series. Using the Hann window reduces

¹Horizons Ephemeris Service: NASA Jet Propulsion Laboratory. <https://ssd.jpl.nasa.gov/horizons/app.html>. Accessed:19.10.2021.

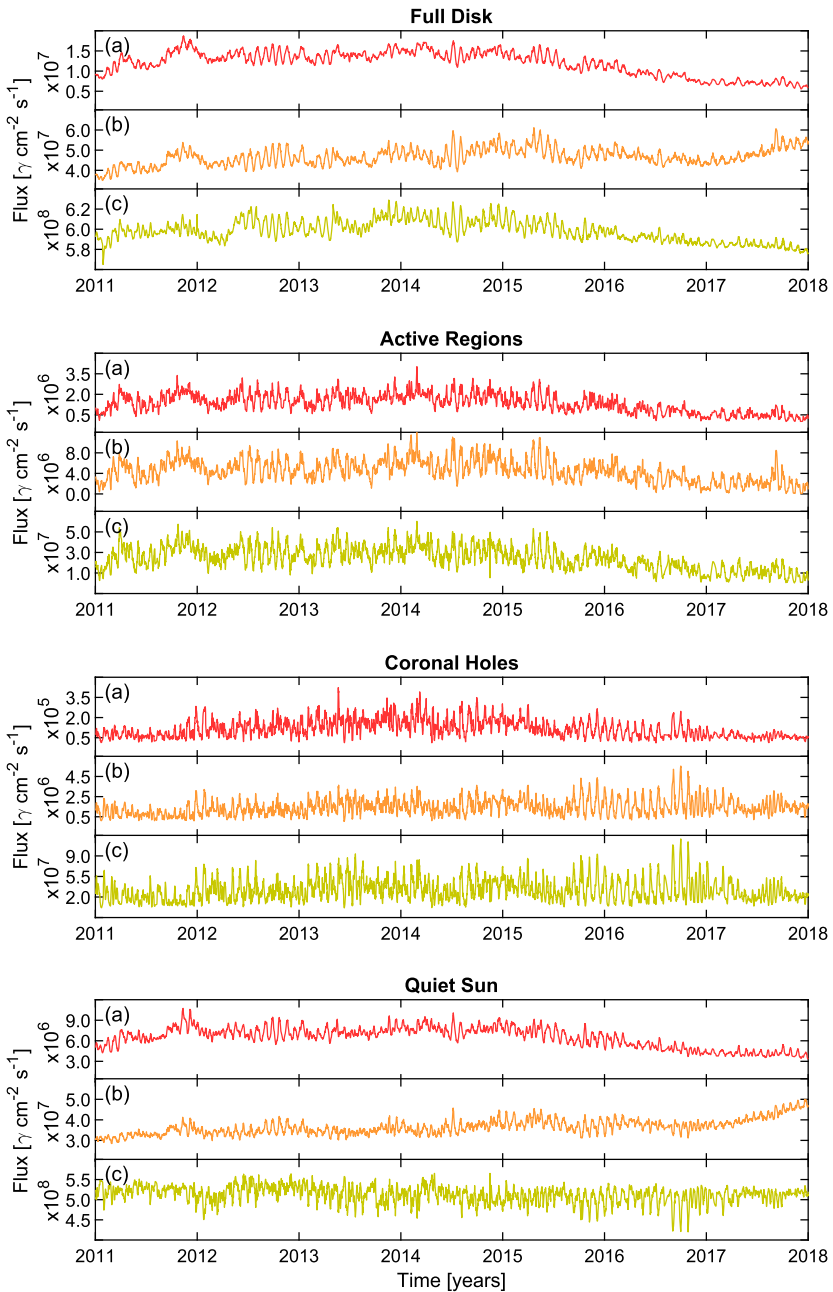


Figure 1 Time-series of the total irradiance from the corona (19.3 nm, sub-panel a in red), the chromosphere (30.4 nm, sub-panel b in orange) and the photosphere (170 nm, sub-panel c in yellow). The top panel shows the full disk, while the three other panels, below each sub-panel, show the segmented areas: active regions, coronal holes, and quiet-Sun from top to bottom, respectively. γ stands for photons.

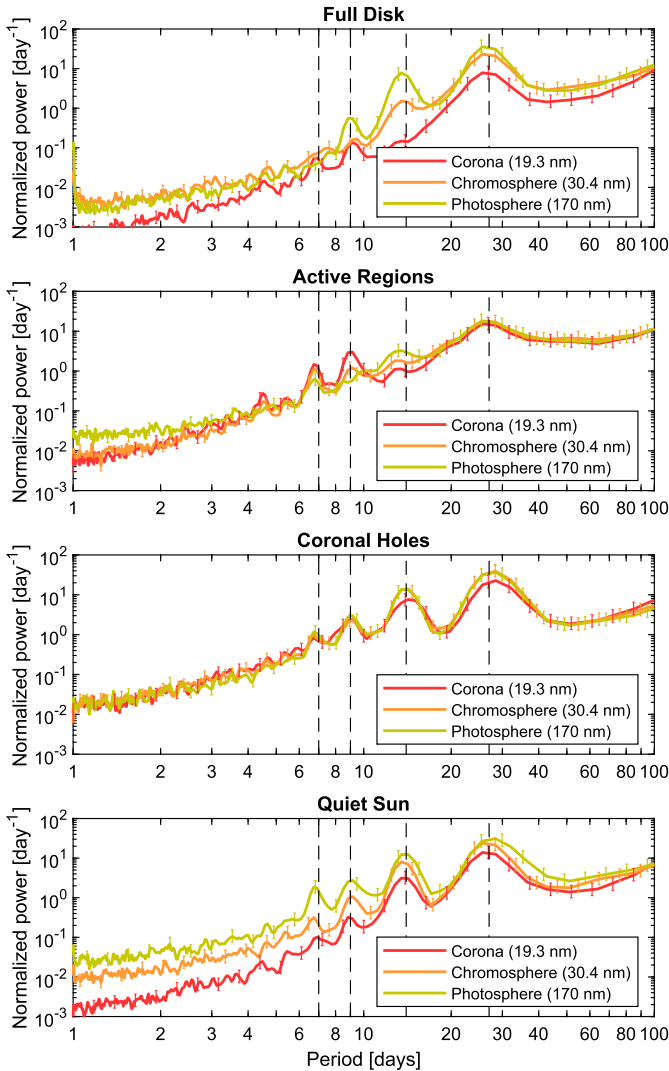


Figure 2 Normalized power spectral density from the total irradiance time series of each of the three atmospheric layers (corona in red, chromosphere in orange, and photosphere in yellow) for the full disk, active regions, coronal holes, and the quiet Sun from top to bottom, respectively. The error bars show the 95% confidence level (i.e. 2σ). The error bars of the different layers are staggered to avoid visual overlap. The vertical dashed lines indicate the periods of 7, 9, 14, and 27 days.

the artifacts due to discontinuities of the signal at the edges of the window, while the detrending helps remove artificial power at 0 Hz (i.e. offset) from the spectral analysis. The final PSD is obtained by combining the power spectral density of all segments. Although this method reduces the longer periodicity available, it provides a better estimation of the PSD. To compare different atmospheric layers, the time series were normalized before performing the spectral analysis. This was achieved by removing the mean of each time series and dividing by its standard deviation. The power spectral densities for the full disk, active regions,

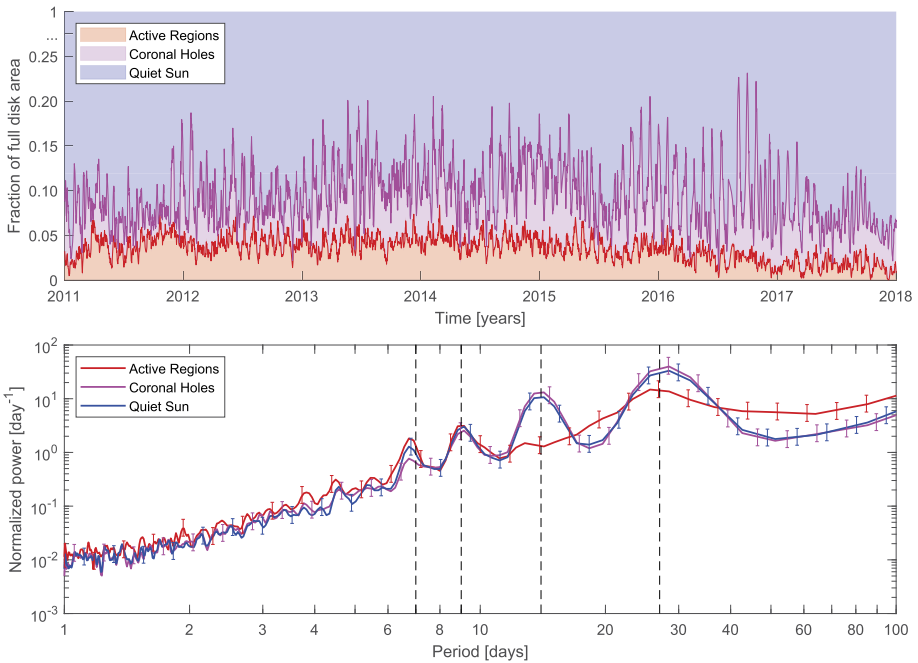


Figure 3 Top panel: Fraction of the full disk taken by the active regions (red shaded area), the coronal holes (magenta shaded area), and the quiet Sun (blue shaded area). Note that the y-axis is discontinuous, as the quiet Sun always covers more than 80% of the disk total area. Bottom panel: Normalized power spectral density from the area time-series of active regions (red), coronal holes (magenta), and the quiet Sun (blue). Note that the periodicities in the quiet-Sun area are by design introduced by the periodicities in the active regions and coronal holes. The vertical dashed lines indicate the periods of 7, 9, 14, and 27 days.

coronal holes, and quiet Sun are shown in Figure 2. A significant amplitude for periods at 7, 9, and 27 days can be observed in the full-disk irradiance of the corona, while peaks at 9, 14, and 27 days are more prominent in the full-disk irradiance of the chromosphere and the photosphere. On one hand, apart from the peak in 27 days seen in all layers, only the peaks coming from active regions in the corona at 7 and 9 days can be seen in the irradiance, while at 14 days the power increases in both the chromosphere and the photosphere. On the other hand, peaks at 7, 9, 14, and 27 days are seen in the irradiance from coronal holes and the quiet Sun in all three layers. Notice that the broadening of the peaks is partially a side effect of using the Hann window.

Such periodicities are commonly seen in the literature: the broad peak around 27 days corresponds to the solar rotation (between 24 days at the equator and up to 38 days at the poles, averaging at around 27 days), and the lower periods are equal to its higher harmonics ($27/2 = 13.5$ days, $27/3 = 9$ days, and $27/4 = 6.5$ days). Some authors (Emery et al., 2011; Efremov, Parfinenko, and Solov'ev, 2018; Pap, Tobiska, and Bouwer, 1990; Nikonova, Klocheck, and Palamarchuk, 1998) interpreted these lower periods and related them to the solar interior and to possible gravity modes of the Sun (g -modes). The segmentation of the images provides a much simpler explanation to these high-order harmonics as demonstrated hereafter.

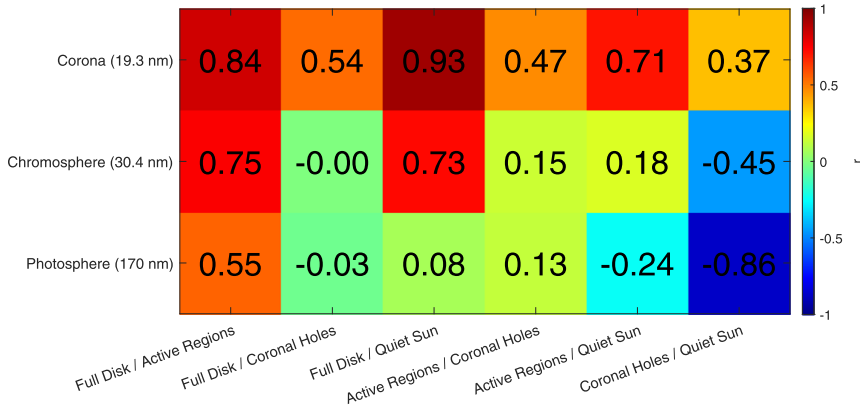


Figure 4 Correlation coefficient between the different features for each of the atmospheric layers (top: corona, middle: chromosphere, bottom: photosphere).

4. Investigating the Higher-Order Harmonics

The segmentation analysis also provides time series of the area covered by active regions and coronal holes. The top panel of Figure 3 shows the fraction of the total solar disk covered by the two, while the remaining part belongs to the quiet Sun. Using the same spectral analysis on these time series reveals similar peaks in each periodicity as shown in the bottom panel of Figure 3. This suggests that the periodicities are not so much linked to the irradiance output of the Sun per se but rather to the change in area of the feature on its surface. This would directly explain the periodicities seen in the irradiance of the active regions and coronal holes, and indirectly of the quiet Sun (as the total area of all three are linked by construction in our analysis). Furthermore, the connection between the periodicities of the active region areas and the full disk irradiance can be explained by the correlation between the total irradiance time series of the different features. Figure 4 shows the correlation coefficients for the three different atmospheric layers. One can see the relatively high correlations between the active regions and the full disk (0.84, 0.75, and 0.55 for the corona, chromosphere and photosphere, respectively). This can be interpreted by the variability of the active regions as the main contributors to the variability of the full disk. Hence, one can say that observing the full disk is a relatively good proxy for assessing the variability of the active regions, which are directly affected by their area on the disk. Note that the quiet Sun also appears to have a relatively high correlation with the full disk at coronal and chromospheric levels (0.93 and 0.73, respectively). This can be a result of the uncertainty in the segmentation, not classifying all ephemeral regions/bright points as active regions (thus being added to the quiet Sun), which could also contribute to the irradiance variability of the full disk. The low correlation coefficient between the full disk and the quiet Sun in the photosphere supports this assumption, as the ephemeral regions/bright points are only prominently seen above the photosphere.

In summary, it appears that the periodicities seen in the full disk total irradiance can be attributed to the change in area of active regions on the solar surface. This is supported by the fact that the same periodicities are seen in the time series of the total area covered by active regions and that the total irradiance of active regions is correlated to the total irradiance of the full disk.

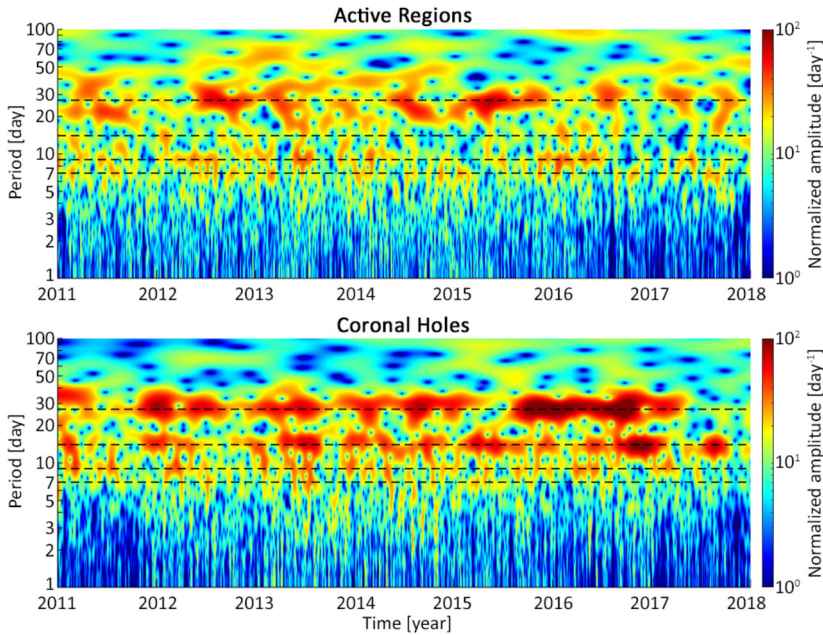


Figure 5 Wavelet analysis of the area time-series for active regions (top panel) and coronal holes (bottom panel). Horizontal black dashed lines indicate the periods of 7, 9, 14, and 27 days.

5. Looking for Underlying Periodicities of the Periodicity Peaks

The nature of the periodicity peaks seen in the bottom panel of Figure 3 is investigated further by performing a Morse wavelet analysis of the two time series (continuous wavelet transform (cwt) MATLAB package, Lilly and Olhede, 2012) for the area of active regions and coronal holes, respectively. The wavelet analysis shown in Figure 5 reveal that the peaks in periodicities at 27, 14, 9, and 7 days are not continuously present. Extracting a time series of the power for each peak and performing a spectral analysis reveal a power spectral density without particular peaks as shown in Figure 6. This is very similar to a random signal; thus, it can be concluded that there are no underlying periodicities governing the occurrence of a periodicity peak in the areas of active regions or coronal holes.

6. Modeling the Periodicities

A simple toy-model was created to reproduce periodicities seen in the area variation of the active regions. An active region was represented as a dot on a rotating circle, and the change in area as the dot moves in front of the observer was calculated as the cosine of the line-of-sight angle. The area for the dot is set to zero when it is not on the observer's side. This is a very simple mathematical approximation for active regions, but it is definitely quite close to reality. The only difference is that all dots have the same size in the toy model, whereas, in practice, the area of active regions can largely vary. Figure 7 shows the area signals and power spectral densities for three different cases of rotating active regions: one single active region, two active regions separated by 180° each, and three active regions separated by 120° each. The higher-frequency harmonics of the rotation are clearly seen and are due

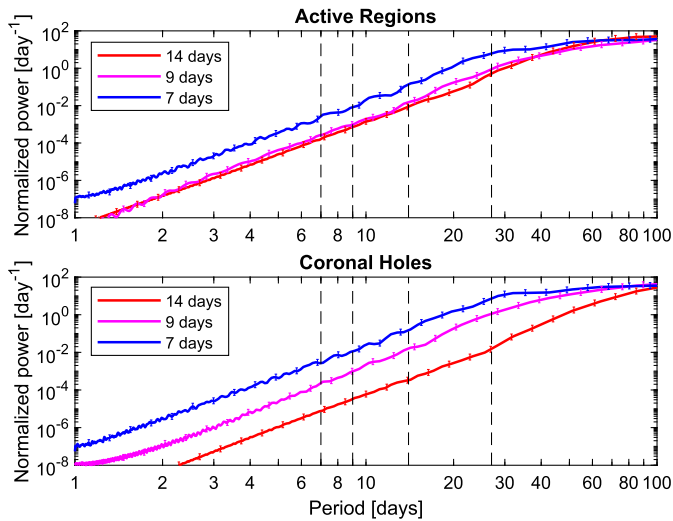


Figure 6 Normalized power spectral density from the periodicity time-series at 14, 9, and 7 days extracted from Figure 5. The vertical dashed lines indicate the periods of 7, 9, 14, and 27 days. No particular periodicity peaks are seen, which indicates that the underlying mechanism producing them is likely to be random. The error bars show the 95% confidence level (i.e., 2σ). The error bars of the different layers are staggered to avoid visual overlap.

to the clipped signal of the visible area. The visible area of a given active region goes to zero when it goes out of the observer's field of view, thus cropping the perfect sine wave of the area signal for this active region. This cropped sine-wave gives rise to the higher-order harmonics. Adding additional active regions around the disk removes the lower frequency peak, starting from the rotation frequency itself, but maintains the higher order peaks. Interestingly, only even and not odd harmonics are seen (i.e. at 14 days, 7 days, etc., but not 9 days, 5.4 days, etc.). However, the odd harmonics can be induced by changing the exponent of the cosine, i.e. the projection function of the active region. This is shown in Figure 8, where a single spot is simulated rotating around the circle with various powers of the cosine function from 1 (i.e. same as Figure 7) down to 0.3. Lower exponents also seem to increase the power of the peaks at higher frequencies. In practice, this exponent can be related to the line-of-sight and limb brightening/darkening effects, affecting the segmentation methods from which the area of the active regions are obtained. A particular example is the vertically extending features of the active region in the corona, such as loops and prominences, which are included in the segmentation. Such features do not increase the area at the disk center, where they are seen from above, but can contribute to a larger segmented area as the active regions moves towards the limb (until a cut-off at the limb, as regions beyond the solar disk are not considered in the analysis).

This simple toy-model was further refined in an attempt to reproduce the time series of the active region areas observed by AIA. In order to reproduce the solar cycle variation seen from 2011 to 2018, the number of active regions around the disk was adjusted to match the variation from the total sunspot number during this period (daily sunspot number taken from the Sunspot Index and Long-term Solar Observations (SILSO) World Data Center (2021) smoothed with a 20-day moving average filter). A factor of 1/6 was applied, as most of the active regions segmented by SPoCA in the corona often include multiple sunspots. The model was initialized by adding a number of active regions matching the sunspot number

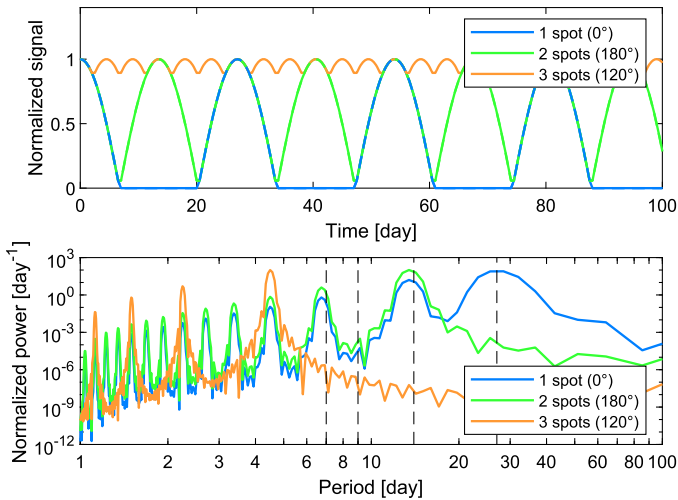


Figure 7 Top panel: Simple area signal generated by rotating one (blue), two (green), and three (orange) spots around the disk. Bottom panel: Corresponding normalized power spectral density of the area signal. The vertical dashed lines indicate the periods of 7, 9, 14, and 27 days.

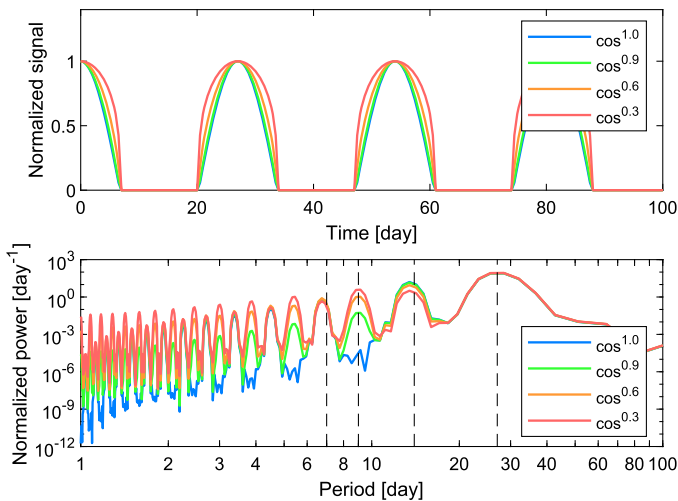


Figure 8 Top panel: Simple area signal generated by rotating one spot around the disk with different exponent affecting the projection function (i.e. cosine). Bottom panel: Corresponding normalized power spectral density of the area signal. The vertical dashed lines indicate the periods of 7, 9, 14, and 27 days.

from 1 January 2011 randomly distributed around the disk. Then, for each consecutive days, new active regions were added if the number of active region still present on the disk was less than the observed sunspot number for this given day. This way, the number of active regions simulated always followed the actual observed sunspot number on the 2011–2018 period. The bottom panel of Figure 9 shows the number of simulated active regions; approximately

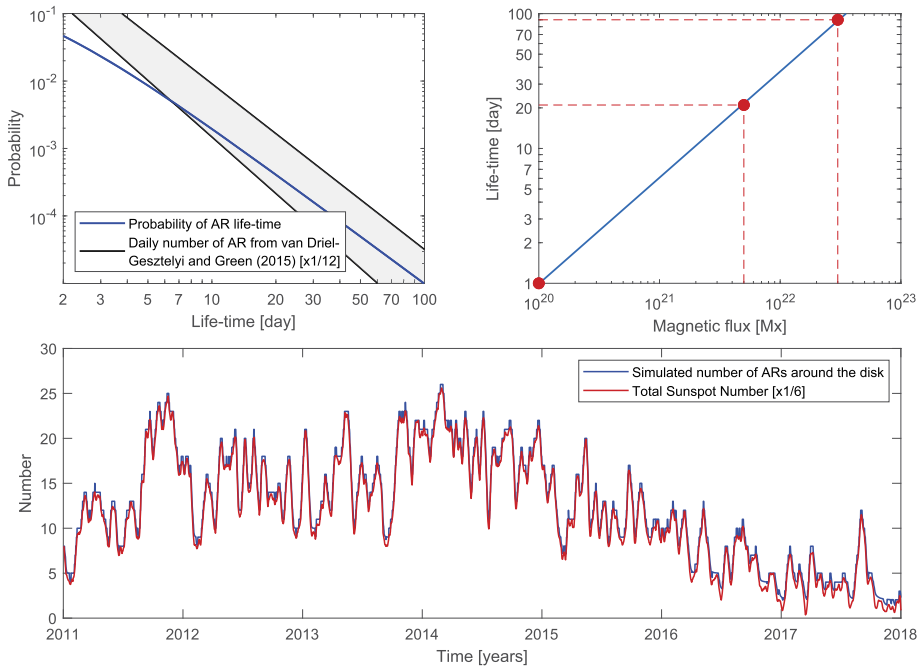


Figure 9 Top-left panel: Comparison between the log-logistic probability distribution function ($\alpha = 1$, $\beta = 4/3$) used to draw the active regions lifetime (blue line) and the upper and lower limits of the number of daily observed active regions from van Driel-Gesztelyi and Green (2015) (shaded grey area between the two solid black lines divided by 12 to account for the mean daily number of observed active regions). Top-right panel: Relationship between the active region magnetic flux and lifetime, as adapted from Table 1 in van Driel-Gesztelyi and Green (2015). The red dots and dashed lines show the three points considered for the fitting: 1, 21, and 90 days corresponding to fluxes of 1×10^{20} , 5×10^{21} , and 3×10^{22} Mx, respectively. Bottom-panel: Number of simulated active regions around the disk (blue line), compared to the total daily sunspot number observed from 2011 to 2018 (red line, x1/6 taken from the Sunspot Index and Long-term Solar Observations (SILSO) World Data Center (2021) smoothed with a 20-day moving average filter).

25 of them were present around the full simulated disk during solar maximum, a number comparable to the number of active regions observed in the segmented maps.

The lifetime of each of the generated active regions was randomly drawn from a probability distribution based on Figure 3 from van Driel-Gesztelyi and Green (2015), where the daily probability of observing an active region with a given magnetic flux is presented. Table 1 in van Driel-Gesztelyi and Green (2015) indicates that small active regions with magnetic flux between 1×10^{20} and 5×10^{21} Mx have lifetimes from days to weeks, while large active regions with flux from 5×10^{21} to 3×10^{22} Mx have lifetimes from weeks to months. Considering “day” as 1 day, “weeks” as 21 days, and “months” as 90 days, a logarithmic relationship between the active regions lifetimes and their magnetic flux was estimated (shown in the top-right panel of Figure 9). This relationship was used to convert the daily number of active regions with a given magnetic flux into the daily number of active regions with a given lifetime. The probability of an active region to have a given lifetime is then calculated by dividing by the total daily number of active regions around the disk. The daily number of active regions varies during the solar cycle (see bottom panel of Figure 9), but, here, for simplicity its average value of ≈ 12 for the 2011–2018 period was considered.

A simple approach to obtain this probability distribution is to fit a log–log linear relationship directly between the upper and lower limits observed in Figure 3 in van Driel-Gesztelyi and Green (2015). However, it was observed that the power spectral density resulting from using such probability distribution does not match the observed power spectral density for the area of active regions. Indeed, in that case a higher power is seen at shorter periods (≤ 5 days) while less power is observed at longer periods (≥ 20 days). The better match was found with a log-logistic distribution with $\alpha = 1$ and $\beta = 4/3$. This probability distribution function has a less inclined tail for periods ≥ 10 days and also tapers off for periods below 5 days compared to the log–log linear probability distribution. This consequently increases the number of active regions with longer lifetimes thus contributing to higher power at periods ≥ 20 days, reducing the number of short-living active regions and decreasing the power at periods ≤ 5 days. The top-left panel of Figure 9 shows the used log-logistic distribution compared to the observed upper and lower log–log linear limits from Figure 3 in van Driel-Gesztelyi and Green (2015). Notice that the probability distribution function was truncated for the values below 2 days, as active regions with shorter lifetime were not considered here. It is important to point out that there are no particular physical motivations for using a log-logistic distribution besides its fitting shape. However, its simple parametrization makes it easy to use and reproduce.

Finally, an exponent of 0.5 on the cosine for the line-of-sight projection was used to obtain the contribution of the active regions to the simulated area signal. The resulting time series was then normalized to the same mean as the observed active region areas from 2011 to 2018. Notice that in order to keep the model simple, the size/weight of the active regions was kept constant regardless of their lifetime. In practice, this is probably different, as longer living active regions have larger magnetic flux and therefore likely larger area. However, a clear relationship between magnetic field and active region areas is difficult to estimate because active regions in the corona might be complex (e.g., they might have multiple loops), and they would also evolve and merge during their lifetime.

The simulation was repeated $N = 10^3$ times, each time a different time series for the area of active regions was generated, for which a spectral analysis was conducted.

In conclusion, a similar power spectral density as observed for the active region areas could be reproduced as shown in Figure 10. The model reproduces periodicity peaks at 7 and 9 days within a 3σ overlap with the observed peaks and also indicates that such large-power peaks are unlikely to appear over longer periods of time. Indeed, apart from the main peak at 27 days, the signature of the other peaks in periodicities is very weak in the mean power spectral density out of the $N = 10^3$ simulations.

Although the model is by no means a perfectly accurate description of how active regions emerge and evolve, it provides additional insights on the nature of power spectral densities of active regions. Firstly, the presence of short living active regions (≤ 7 days) appeared to be important to account for the overall power at low periods. Secondly, although the long-living active regions (≥ 14 days) are the main contributors to the higher harmonics of the solar rotation, it was observed that a too large number of them around the disk actually damps the power of these peaks, i.e. dilutes the effect.

7. Conclusions

Long-term periodicities in the solar irradiance are often observed with periods proportional to the solar rotational period of 27 days. The origin of these periods are linked to the solar interior and possibly to gravity modes of the Sun as argued by some authors (Emery et al.,

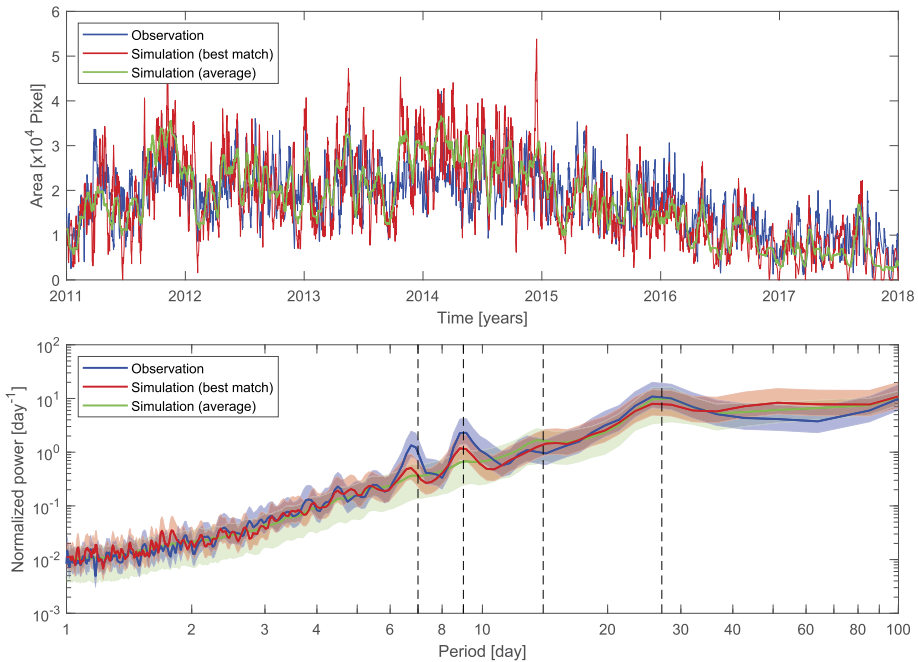


Figure 10 Top panel: Example of area signal generated with the refined model (red, time series with the best matching power spectral density) compared to the observed active region areas (blue). The average area out of the $N = 10^3$ time series is shown in green. Bottom panel: Normalized power spectral density of the observed active region areas from 2011 to 2018 (blue) compared to the best matching power spectral density (red) and the average power spectral density (green) obtained from the $N = 10^3$ simulated time series. The shaded areas show the 3σ error interval (i.e. 99.97%). The vertical dashed lines indicate the periods of 7, 9, 14, and 27 days.

2011; Efremov, Parfinenko, and Solov'ev, 2018; Pap, Tobiska, and Bouwer, 1990; Nikonova, Klocheck, and Palamarchuk, 1998). However, these periods are also direct higher harmonics of the rotation, but their origin, as such, is rarely discussed further. These periodicities at 27, 14, 9, and 7 days were observed in the various bands of SDO/AIA from corona to chromosphere and photosphere (19.3, 30.4, and 170 nm, respectively) when integrating full disk images for a 7-year period from 2011 to 2018 (6 images per day). For each of these images, the SPoCA segmentation software was used to produce maps of the active regions and coronal holes. This provided a way to extract the irradiance emitted from these two classes of features and to obtain time series of the observed area covered by both classes during the 7-year period. A spectral analysis of these area time-series revealed similar peaks in periodicities, indicating that the higher harmonics seen in the full-disk irradiance are introduced by the change in area of the rotating features on the solar surface. This explanation is further supported by the relatively high correlation between the total flux of active regions and the full disk total flux, in particular, at chromospheric and coronal heights. This can be interpreted as that the active region variability is the main contributor to the full disk variability as it was also reported previously by Kumara et al. (2014). A simple toy-model was made to investigate the periodicities seen in the area time-series. Active regions were represented as a spot on a rotating circle and generated based on the total sunspot number from 2011 to 2018 with a lifetime randomly drawn from a probability distribution (taken as a log-logistic

distribution with $\alpha = 1$, $\beta = 4/3$, truncated for the values below 2 days), which matched the distribution of active regions sizes observed by other authors. The change in area for each active region, i.e. projection function, was calculated as the cosine of the angle to the fixed observer taken to the power of 0.5 and set to zero when outside the field-of-view. Adjusting the projection function with an exponent was observed to be important, as the odd harmonics (e.g., 9 days) would not otherwise appear. In practice, this exponent can be understood as representing line-of-sight and limb brightening/darkening effects, affecting the segmentation method, from which the area of the active regions is obtained. Using this simplified model for the emergence and evolution of active regions, similar peaks in the periodicities as seen in the observations could be reproduced.

In summary, the periodicities in the order of days seen in the solar irradiance are higher-harmonics of the solar rotation, which are induced by the change in area of the features on the solar disk; this are detected in the area of the active regions from 2011 to 2018 and reproduced with a simple modeling of the active region lifetimes around the Sun. The harmonics arise due to the clipping of the signal as active regions disappear behind the Sun. Moreover, we did not detect any underlying periodicity, driving the occurrence of a peak, indicating that for periods below one solar rotation, the formation of active regions follows a random process. It, therefore, seems unlikely that these periods are related to processes in the interior of the Sun.

Acknowledgements The solar EUV/UV images used in this paper have been obtained with SDO/AIA instrument. Some of the authors (G.G. and R.K.) visited ESTEC Faculty several times to work with J.Z. during this research period and their visits were sponsored by ESTEC. They wish to express their sincere thanks to the ESTEC Faculty for the financial support. During this research period R.K. visited CNRS/LATMOS (France) and ISEE/Nagoya University (Japan), and he expresses his sincere thanks to Luc Damé, Kanya Kusano (Director of ISEE), and Shinsuke Imada for the discussion and support provided. Finally we would like to express our deepest thanks to the anonymous referee who reviewed the article, as the provided feedback greatly improved the quality of the article.

Funding Note Open access funding provided by Royal Institute of Technology.

Declarations

Disclosure of Potential Conflicts of Interest The authors declare that there are no conflicts of interest

Open Access This article is licensed under a Creative Commons Attribution 4.0 International License, which permits use, sharing, adaptation, distribution and reproduction in any medium or format, as long as you give appropriate credit to the original author(s) and the source, provide a link to the Creative Commons licence, and indicate if changes were made. The images or other third party material in this article are included in the article's Creative Commons licence, unless indicated otherwise in a credit line to the material. If material is not included in the article's Creative Commons licence and your intended use is not permitted by statutory regulation or exceeds the permitted use, you will need to obtain permission directly from the copyright holder. To view a copy of this licence, visit <http://creativecommons.org/licenses/by/4.0/>.


References

- Barra, V., Delouille, V., Hochedez, J.F.: 2008, *Adv. Space Res.* **42**(5), 917. DOI.
- Barra, V., Delouille, V., Kretzschmar, M., Hochedez, J.-F.: 2009, *Astron. Astrophys.* **505**(1), 361. DOI.
- Barth, C.A., Tobiska, W.K., Rottman, G.A.: 1990, *Geophys. Res. Lett.* **17**(6), 571.
- Donnelly, R.F., Heath, D.F., Lean, J.: 1982, *J. Geophys. Res.* **87**(10), 318.
- Donnelly, R.F., Heath, D.F., Lean, J., Rottman, G.: 1983, *J. Geophys. Res.* **88**, 9883.
- Efremov, V.I., Parfinenko, L.D., Solov'ev, A.A.: 2018, *Astrophys. Space Sci.* **363**, 257. DOI.
- Emery, B.A., Richardson, I.G., Evans, D.S., Rich, F.J., Wilson, G.R.: 2011, *Solar Phys.* **274**, 399. DOI.

- Kumara, S.T., Kariyappa, R., Dominique, M., Berghmans, D., Damé, L., Hochedez, J.-F., Doddamani, V. H., Chitta, L. P.: 2012, *Adv. Astron.* **5**. DOI.
- Kumara, S.T., Kariyappa, R., Zender, J.J., Giono, G., Delouille, V., Chitta, L.P., Damé, L., Hochedez, J.-F., Verbeeck, C., Mampaey, B.: 2014, *Astron. Astrophys.* **591**, A9. DOI.
- Lean, J., Brueckner, G.E.: 1988, *Astrophys. J.* **337**, 568.
- Lemen, J.R., et al.: 2012, *Solar Phys.* **275**, 17. DOI.
- Lilly, J.M., Olhede, S.C.: 2012, *IEEE Trans. Signal Process.* **60**(11), 6036. DOI.
- Nikonova, M.V., Klocheck, N.V., Palamarchuk, L.E.: 1998, In: Deubner, F.L., et al. (eds.) *Proc. IAU* **185**, 119. DOI.
- Pap, J., Tobiska, K.W., Bouwer, D.S.: 1990, *Solar Phys.* **129**, 165.
- Pesnell, W.D., Thompson, B.J., Chamberlin, P.C.: 2011, In: Chamberlin, P., Pesnell, W.D., Thompson, B. (eds.) *The Solar Dynamics Observatory*, Springer, New York. DOI.
- Rottman, G.J.: 1983, *Planetary Space Sci.* **31**, 1001.
- Rottman, G.J., London, J.: 1984 *Proc. Int. Radiation Symp., Perugia, Italy*, 320.
- Simon, P.C.: 1982 *Proc. Symp. on the Solar Constant and the Spectral Distribution of Solar Irradiance, Boulder, Colorado*, 50.
- Simon, P.C., Rottman, G.J., White, O.R., Knapp, B.: 1987, Solar radiative output variation. In: Foukal, P. (ed.) *Proc. Workshop 9–11 Nov. 1987*, National Center for Atmospheric Research, Boulder, 125.
- Sunspot Index and Long-term Solar Observations (SILSO) World Data Center: International Sunspot Number Monthly Bulletin and online catalogue. <http://www.sidc.be/silso>. Accessed: 19.10.2021.
- Tobiska, K.W., Bouwer, D.S.: 1989, *Geophys. Res. Lett.*, 779. DOI.
- van Driel-Gesztelyi, L., Green, L.M.: 2015, *Living Rev. Solar Phys.* **12**, 1. DOI.
- Verbeeck, C., Delouille, V., Mampaey, B., De Visscher, R.: 2014, *Astron. Astrophys.* **561**, A29. DOI.
- Zender, J.J., Kariyappa, R., Giono, G., Bergmann, M., Delouille, V., Damé, L., Hochedez, J.-F., Kumara, S.T.: 2017, *Astron. Astrophys.* **605**, A41.

Publisher's Note Springer Nature remains neutral with regard to jurisdictional claims in published maps and institutional affiliations.

Authors and Affiliations

G. Giono¹  · J.J. Zender² · R. Kariyappa^{3,4} · L. Damé⁵

✉ G. Giono
ggiono@kth.se

¹ Division of Space and Plasma Physics, KTH-Royal Institute of Technology, Stockholm, Sweden

² European Space Research and Technology Center (ESTEC), European Space Agency (ESA), Noordwijk, The Netherlands

³ Indian Institute of Astrophysics, Bangalore, India

⁴ Institute for Space-Earth Environmental Research, Nagoya University, Nagoya, Japan

⁵ Laboratoire Atmosphères, Milieux, Observations Spatiales (LATMOS), CNRS, Paris-Saclay University, Guyancourt, France